J|A|C|S
ARTICLES
Published on Web 09/03/2003

Molecular Dynamics Simulation of an Electric Field Driven Dipolar Molecular Rotor Attached to a Quartz Glass Surface

Dominik Horinek and Josef Michl*

Contribution from the Department of Chemistry and Biochemistry, University of Colorado at Boulder, Boulder, Colorado 80309-0215

Received February 26, 2003; E-mail: horinek@eefus.colorado.edu; michl@eefus.colorado.edu

Abstract: Molecular dynamics simulations of the response of a dipolar azimuthal 3-chloroprop-1-ynyl rotor mounted on the surface of quartz glass to a rotating electric field were performed. The rotor motion was classified as synchronous, asynchronous, random, or hindered, based on the value of the average lag of the rotor behind the field and a comparison of the intrinsic rotational barrier V_b with kT. A phase diagram of rotor behavior was deduced at 10, 300, and 500 K as a function of field strength and frequency. A simple model for the rotor motion was developed, containing the driving force, the temperature, the height of the torsional barrier, and the friction constant of the rotor. Defining E_{bo} to be the electric field strength necessary to get rotational response from the rotor ("breakoff field") and μ to be the rotor dipole moment component in the plane of rotation, we find that E_{bo} is frequency independent when $2\mu E_{bo}$ is less than either V_b or kT (the driving force needs to overcome the more important of the two, the intrinsic barrier or random thermal motion). At higher frequencies, E_{bo} is a quadratic function of the frequency and the driving force fights friction, which is dictated by intramolecular vibrational redistribution (IVR) from the pumped rotational mode to all others. Fitting the simple model to simulation data, we derived a friction constant of 0.26 ps eV $\times$ (ν − 0.5)/THz between 500 and 1000 GHz.

Introduction

The notion of molecular sized machinery is an important part of nanotechnology,[1,2] albeit subject to significant thermodynamic constraints.[3] Various approaches to such machines have been proposed, and the one of interest to us is the application of synthetic chemistry to build them from molecular construction kits[4,5] and to include rotating parts.[6−8] Directional rotation is particularly useful when the axis of rotation is fixed in space and oriented along a preferred direction, and we have therefore concentrated on the development of molecular rotors attached to a surface either randomly or in a regular array. The former have been subject of both computer simulations[9−11] and experimental study.[11] Some progress toward the synthesis and characterization of arrays has also been achieved.[5,12−15]

Many other investigators have been interested in molecular rotors on surfaces,[16−18] in solution,[19−24] inside crystals,[25−27] and in the gas phase,[28] and very large molecular motors based on proteins play an important role in nature.[29−31] However, little is known in detail about how surface-mounted rotors or similar molecular-size machinery would respond to attempts to drive them mechanically or electrically.

(1) Balzani, V.; Credi, A.; Raymo, R. M.; Stoddart, J. F. *Angew. Chem., Int. Ed.* **2000**, *39*, 3348.
(2) Sauvage, J.-P., Ed. *Molecular Machines and Motors*; Springer: Berlin, 2001.
(3) Evans, D. J. *Adv. Phys.* **2002**, *51*, 1529.
(4) Kaszynski, P.; Michl, J. *J. Am. Chem. Soc.* **1988**, *110*, 5225.
(5) Michl, J.; Kaszynski, P.; Friedli, A. C.; Murthy, G. S.; Yang, H.-C.; Robinson, R. E.; McMurdie, N. D.; Kim, T. In *Strain and its Implications in Organic Chemistry*; de Meijere, A., Blechert, S., Eds.; NATO ASI Series, Vol. 273; Kluwer Academic Publishers: Dordrecht, The Netherlands, 1989; p 463.
(6) Kaszynski, P.; Friedli, A. C.; Michl, J. *J. Am. Chem. Soc.* **1992**, *114*, 601.
(7) Harrison, R. M.; Magnera, T. F.; Vacek, J.; Michl, J. In *Modular Chemistry*; Michl, J., Ed.; Kluwer: Dordrecht, The Netherlands, 1997; p 1.
(8) Han, J.; Globus, A.; Jaffe, R.; Deardorff, G. *Nanotechnology* **1997**, *8*, 186.
(9) Vacek, J.; Michl, J. *New J. Chem.* **1997**, *21*, 1259.
(10) Vacek, J.; Michl, J. *Proc. Natl. Acad. Sci. U.S.A.* **2001**, *98*, 5481.
(11) Clarke, L. I.; Horinek, D.; Kottas, G. S.; Varaksa, N.; Magnera, T. F.; Hinderer, T. P.; Horansky, R. D.; Michl, J.; Price, J. P. *Nanotechnology* **2002**, *13*, 533.
(12) Magnera, T. F.; Pecka, J.; Vacek, J.; Michl, J. In *Nanostructural Materials: Clusters, Composites, and Thin Films*; Moskovits, M., Shalaev, V., Eds.; ACS Symposium Series 679; American Chemical Society: Washington, DC, 1997; p 213.
(13) Magnera, T. F.; Pecka, J.; Michl, J. In *Science and Technology of Polymers and Advanced Materials*; Prasad, P. N., Mark, J. E., Kandil, S. H., Kafafi, Z. H., Eds.; Plenum: New York, 1998; p 385.
(14) Varaksa, N.; Pospíšil, L.; Magnera, T. F.; Michl, J. *Proc. Natl. Acad. Sci. U.S.A.* **2002**, *99*, 5012.
(15) Michl, J.; Magnera, T. F. *Proc. Natl. Acad. Sci. U.S.A.* **2002**, *99*, 4788.
(16) Gimzewski, J. K.; Joachim, C.; Schlitter, R. R.; Langlais, V.; Tang, H.; Johannsen, I. *Science* **1998**, *281*, 531.
(17) Hersam, M. C.; Guisinger, N. P.; Lyding, J. W. *Nanotechnology* **2000**, *11*, 70.
(18) Joachim, C.; Gimzewski, J. K. *Struct. Bond.* **2001**, *99*, 1.
(19) Balzani, V.; Gómez-López, M.; Stoddard, J. F. *Acc. Chem. Res.* **1998**, *31*, 405.
(20) Clayden, J.; Pink, J. H. *Angew. Chem., Int. Ed.* **1998**, *37*, 1937.
(21) Sauvage, J. P. *Acc. Chem. Res.* **1998**, *31*, 611.
(22) Koumura, N.; Zijlstra, R. W. J.; van Delden, R. A.; Harada, N.; Feringa, B. L. *Nature* **1999**, *401*, 152.
(23) Bermudez, V.; Capron, C.; Gase, T.; Gatti, F. G.; Kajzar, F.; Leigh, D. A.; Zerbetto, F.; Zhang, S. *Nature* **2000**, *406*, 608.
(24) Kelly, T. R.; Sestelo, J. P. *Struct. Bond.* **2001**, *99*, 19.
(25) Dominguez, Z.; Dang, H.; Strouse, M. J.; Garcia-Garibay, M. A. *J. Am. Chem. Soc.* **2002**, *124*, 2398.
(26) Godinez, C. E.; Zepeda, G.; Garcia-Garibay, M. A. *J. Am. Chem. Soc.* **2002**, *124*, 4701.
(27) Dominguez, Z.; Dang, H.; Strouse, M. J.; Garcia-Garibay, M. A. *J. Am. Chem. Soc.* **2002**, *124*, 7719.
(28) Hoki, K.; Yamaki, M.; Koseki, S.; Fujimura, Y. *J. Chem. Phys.* **2003**, *118*, 497, and references therein.
(29) Jankowsky, E.; Gross, C. H.; Shuman, S.; Pyle, A. M. *Nature* **2000**, *403*, 447.
(30) Yasuda, R.; Noji, H.; Kinosita, K., Jr.; Itoh, H. *Nature* **2001**, *410*, 898.

10.1021/ja0348851 CCC: $25.00 **© 2003 American Chemical Society**

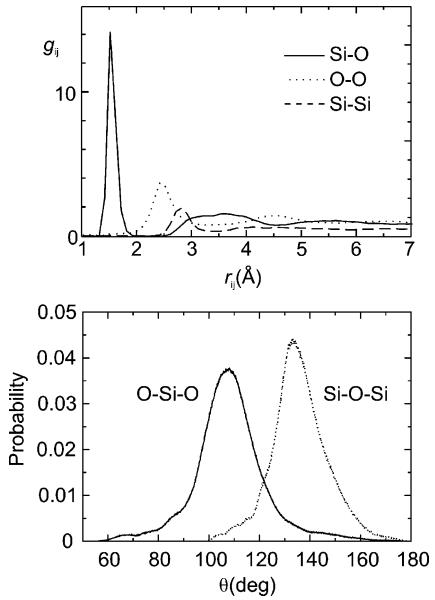

Figure 1. Radial pair distribution functions for pairs of Si−Si, Si−O, and O−O atoms and angle distribution functions for Si−O−Si and O−Si−O angles obtained from the quartz glass model.

Presently, we report the results of molecular dynamics simulations of dipolar 3-chloropropynyl rotors mounted on a quartz glass surface through a silicon atom bridge. This is an extension of earlier work[11] in which chloromethyl rotors were studied experimentally and by molecular dynamics. The motivation for the present work is to study a rotor which is chemically similar and can again be mounted on a quartz surface by small modifications of the same procedure, but has a lower torsional barrier. Furthermore, we extend a previously developed[10] simple "inclined washboard" potential model used to analyze the computer simulations of the rotor motion, in that we explicitly consider intrinsic rotational barriers.

Computational Procedures. A model of a 14 Å thick slab of quartz glass with a surface area of roughly (50 Å)^2, containing approximately 3500 atoms, was created starting with a template structure[32] periodic in the *xy* plane. The model of the quartz glass surface has a density of ∼2.5 g/cm^3. Radial pair distribution functions for Si−Si, Si−O, and O−O pairs and distributions of the Si−O−Si and O−Si−O angles are shown in Figure 1.

One side of the slab was modified to carry the rotor. First, methyl groups were introduced in two ways, referred to as surface I and surface II. Surface I (Figure 2A) was obtained by saturating the free valences arising from the periodicity of the initial template structure by additional Si and O atoms, ensuring that there are only hydroxyl terminal groups on one side of the surface. These surface hydroxyls were then replaced by methyl groups. The unevenness of the surface was in the range of 4 Å. Surface II (Figure 2B) was obtained by constructing a monolayer and attaching it to the quartz glass. The structure of the monolayer was our best guess at the two-dimensional $(-O)_3SiCH_3$ network that results from vapor deposition of trichloromethylsilane on a hydrated quartz glass surface. All methyl groups resided on the same side of the monolayer. A ∼2 Å thick layer was next removed from the top of the quartz glass, yielding Si

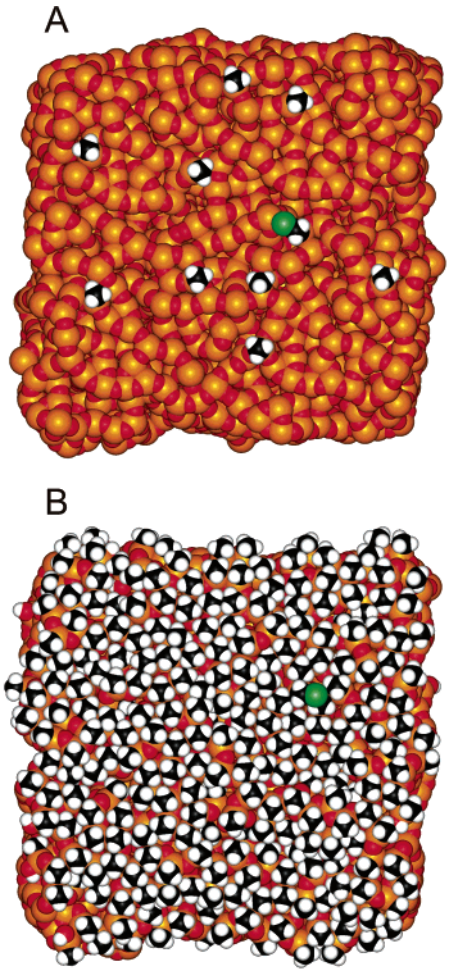

Figure 2. Space filling model of surface I (top) and surface II (bottom).

atoms with one free valence. The attachment of the monolayer to this modified quartz glass surface was done by connecting terminal hydroxyl groups in the monolayer to the free valences of the quartz glass to give Si−O−Si attachments. The unevenness of the monolayer in surface II was mostly below 1 Å. The surface density of methyl groups was 0.04 nm^{-2} on surface I and 9.8 nm^{-2} on surface II.

Second, a rotor was introduced in five different positions on both surfaces by replacing one of five different methyl groups with $-C{\equiv}CCH_2Cl$. In both cases, the five position differed in the angle ξ of inclination of the Si−C≡C−C axis from the surface (Figure 3), which ranged from 49° to 85° (for the *z* axis, $\xi = 90°$).

Charges on the Si and O atoms were calculated by the charge equilibration procedure.[33] For the rotor itself this did not produce satisfactory partial charges in that the Cl atom became very negative and the rotor's dipole moment was clearly exaggerated. A realistic value (1.68 D) of the component of the chloromethyl dipole moment perpendicular to the C−Si axis was obtained from a density functional calculation (B3LYP/6-31G**).[34] Partial charges on the rotor were fitted to the electrostatic potential obtained from this calculation (Table 1).

Torsional potential energy curves were calculated in steps of 5° by fixing one of the Cl−C−Si−O dihedral angles and optimizing all other coordinates, without a cutoff for the

(31) Himmel, D. M.; Gourinath, S.; Reshetnikova, L.; Shen, Y.; Szent-Györgyi, A. G.; Cohen, C. *Proc. Natl. Acad. Sci. U.S.A.* **2002**, *99*, 12645.
(32) *Materials Studio 1.2*; Accelrys: San Diego, CA, 2001.
(33) Rappé, A. K.; Goddard, W. A., III. *J. Phys. Chem.* **1991**, *95*, 3358.

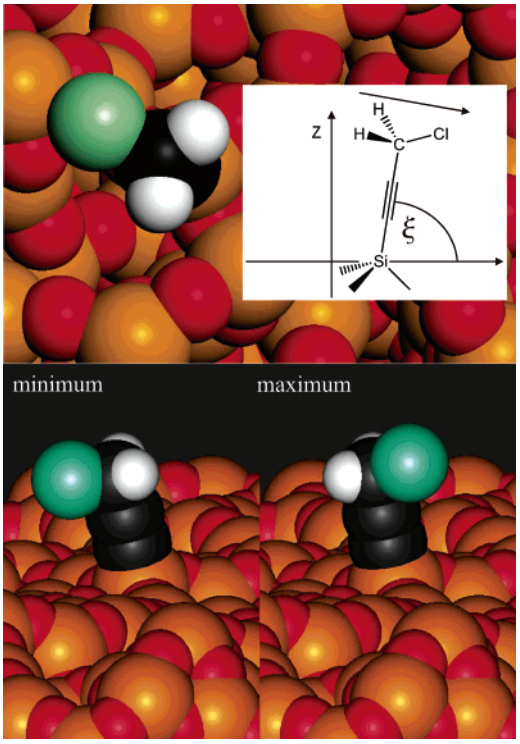

Figure 3. Space filling model of a rotor molecule attached to amorphous SiO_2 surface I. The two bottom structures show the structure at the minimum and the maximum of the torsional potential.

Table 1. Partial Charges of Rotor Atoms Obtained by Fitting to the B3LYP/6-31G** Electrostatic Potential

atom	charge (*e*)
Cl	−0.100
H	−0.211
C (sp^3)	−0.331
C (sp, attached to C)	0.138
C (sp, attached to Si)	−0.258

nonbonding interactions. Of the five rotor positions on surface I, three had potential curves with a single minimum and a single maximum, with barrier heights of 1.5 ($\xi = 56°$), 0.75 ($\xi = 73°$), and 0.65 ($\xi = 75°$) kcal/mol. Two other rotors were more inclined toward the surface and had potential curves with two minima and barriers of 2 ($\xi = 57°$) and 2.5 ($\xi = 49°$) kcal/mol. For the five rotor positions on surface II, we obtained one potential curve with three minima and a barrier height of 1.1 ($\xi = 72°$) kcal/mol and four potential curves with one minimum and barrier heights of 0.9 ($\xi = 81°$), 0.9 ($\xi = 85°$), 2.1 ($\xi = 84°$), and 3.1 ($\xi = 75°$) kcal/mol. The rotor on surface I with a barrier of 0.75 kcal/mol (Figure 3) was chosen for molecular dynamics computations. Its torsional potential is shown in Figure 4.

The TINK molecular dynamics program[9] used is an adaptation of the MOIL code originally written by Elber et al.[35] It

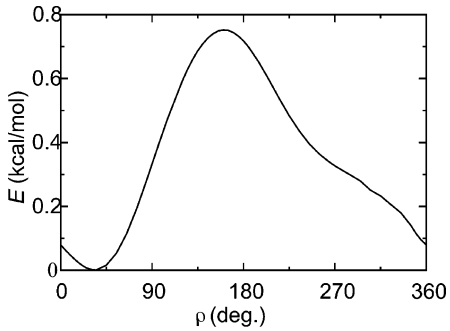

Figure 4. Torsional potential of the rotor used for molecular dynamics simulations.

relies on classical Newtonian dynamics and the universal force field,[36] which is rather approximate but is applicable to all elements of the periodic table. The time step was 1.0 fs. A typical simulation length was 250 ps, but some runs were as long as 1 ns. About 250 simulations were computed in total. A series of simulations without an applied external electric field was run at 10−1500 K. Simulations under the influence of a rotating electric field were performed at 10−1000 K. The field frequency $\nu = \omega/2\pi$ was varied from 10 to 3000 GHz. Most of the simulations were done at 10, 100, 200, 300, 400, and 500 K, and at 10 to 1250 GHz. For each temperature and frequency the field strength was varied to observe the hindered or random, asynchronous and synchronous regimes of rotation. The weakest field was 1 MV/cm, and the strongest, 3×10^2 MV/cm. The field vector rotated in the *xy* plane of the surface, $\boldsymbol{E} = (E \cos \omega t, E \sin \omega t, 0)$.

The application of a strong electric field heats the system, as does occasional conformational relaxation in the glass. To obtain comparable results, we performed the simulation in a canonical ensemble (temperature, volume, and number of particles constant), adjusting atom velocities every 100 time steps to keep a constant system temperature T_{sys}. To avoid effects on the rotor motion, only glass atom velocities were rescaled. A comparison with the results of simulations without velocity rescaling showed that the procedure has no artifactual effect on rotor behavior.

The time-dependent quantities monitored during each simulation run were of several types. The projection of the dipole moment into the *xy* plane, the torsional angle $\rho(t)$, and the lag angle $\alpha(t) = \omega t - \rho(t)$ were recorded. Power spectra of the rotor motion were obtained by Fourier transformation of $\sin \rho(t)$. The time-average lag of the rotor $a = \alpha(t_f)/\omega t_f$ was calculated as an average over the simulation time t_f after an initial equilibration period of 10 ps. The direction of the Si−C bond defined the axis of rotation. All quantities defined with respect to this axis carry the subscript SiC.

The following temperatures were monitored for the $-C{\equiv}CCH_2Cl$ rotor group: (i) The temperature equivalent of the rotational energy of the rotor, $T_{eq}(t) = (1/k)\, I_{SiC}(t)[\bar{\omega}_{SiC}(t)]^2$, where *k* is Boltzmann's constant, $\bar{\omega}_{SiC}(t) = M_{SiC}(t)/I_{SiC}(t)$ is the rotor's instantaneous average angular velocity,

(34) Frisch, M. J.; Trucks, G. W.; Schlegel, H. B.; Scuseria, G. E.; Robb, M. A.; Cheeseman, J. R.; Zakrzewski, V. G.; Montgomery, J. A., Jr.; Stratmann, R. E.; Burant, J. C.; Dapprich, S.; Millam, J. M.; Daniels, A. D.; Kudin, K. N.; Strain, M. C.; Farkas, O.; Tomasi, J.; Barone, V.; Cossi, M.; Cammi, R.; Mennucci, B.; Pomelli, C.; Adamo, C.; Clifford, S.; Ochterski, J.; Petersson, G. A.; Ayala, P. Y.; Cui, Q.; Morokuma, K.; Malick, D. K.; Rabuck, A. D.; Raghavachari, K.; Foresman, J. B.; Cioslowski, J.; Ortiz, J. V.; Stefanov, B. B.; Liu, G.; Liashenko, A.; Piskorz, P.; Komaromi, I.; Gomperts, R.; Martin, R. L.; Fox, D. J.; Keith, T.; Al-Laham, M. A.; Peng, C. Y.; Nanayakkara, A.; Gonzalez, C.; Challacombe, M.; Gill, P. M. W.; Johnson, B. G.; Chen, W.; Wong, M. W.; Andres, J. L.; Head-Gordon, M.; Replogle, E. S.; Pople, J. A. *Gaussian 98*, revision A.9; Gaussian, Inc.: Pittsburgh, PA, 1998.

(35) Elber, R.; Roitberg, A.; Simmerling, C.; Goldstein, R.; Li, H.; Verkhiver, G.; Keasar, C.; Zhang, J.; Ulitsky, A. *Comput. Phys. Commun.* **1994**, *91*, 159.

(36) Rappé, A. K.; Casewit, C. J.; Colwell, K. S.; Goddard, W. A., III; Skiff, W. M. *J. Am. Chem. Soc.* **1992**, *114*, 10 024.

$$I_{SiC}(t) = \sum_{i\in\{R\}} m^i[r_{SiC}{}^i(t)]^2$$

is its instantaneous overall moment of inertia, and

$$M_{SiC}(t) = \sum_{i\in\{R\}} m^i[r_{SiC}{}^i(t)]^2\omega_{SiC}{}^i(t)$$

is its instantaneous overall angular momentum. Here, n specifies the number of atoms in the rotor, m^i is the mass of atom i and $r_{SiC}{}^i(t)$ is the distance between atom i and the SiC axis, while $i \in \{R\}$ specifies that the sum is over all rotor atoms. (ii) The temperature of the fluctuations of the overall angular motion of the rotor as a rigid body with a variable moment of inertia, $T_{fluc}(t) = (1/k)\ I_{SiC}(t)[\bar{\omega}_{SiC}(t) - \langle\bar{\omega}_{SiC}(t)\rangle]^2$, where pointed brackets indicate averaging over the duration of the run. (iii) The rotational temperature

$$T_{rot}(t) = (1/nk)\sum_{i\in\{R\}} I_{SiC}{}^i(t)[\omega_{SiC}{}^i(t) - \bar{\omega}_{SiC}(t)]^2$$

of the rotor in a frame rotating at the rotor's instantaneous overall angular velocity $\bar{\omega}_{SiC}(t)$. The temperature $T_{rot}(t)$ describes the variation in the instantaneous angular velocities of the rotor atoms and is zero for a rigid rotor. (iv) The overall temperature in a frame rotating at $\bar{\omega}_{SiC}(t)$

$$T_{tot}(t) = (1/3nk)\sum_{i\in\{R\}} m^i[v^i(t) - \bar{v}^i(t)]^2$$

where $v^i(t)$ is the velocity vector of atom i and $\bar{v}^i(t)$ is defined by $\bar{v}^i(t) = \bar{\omega}_{SiC}(t) \times r_{SiC}{}^i(t)$. We recognize that the separation of the rotational motion from the overall thermal motion is somewhat ill-defined.

The silicon atom that carried the $-C{\equiv}CCH_2Cl$ substituent was not counted as a part of the rotor. This has no effect on T_{eq}, T_{fluc}, and T_{rot}, which are defined with respect to the Si−C bond as the axis of rotation. It does have a small effect on T_{tot}.

Results

In Table 2 we show results from eight representative simulations, one (A) without, and the others (B−H) with applied electric field. Entry H shows results from a simulation in which nonbonded interactions were turned off. Figures 5, 6, 7, and 8 show the time dependence of T_{eq}, T_{fluc}, T_{rot}, T_{tot}, and $\rho(t)$ obtained from the simulation runs D, E, F, and G.

No Electric Field Applied. At temperatures well below 300 K, kT is not sufficient for the rotor group to overcome the intrinsic rotational barrier V_b within the ∼0.5 ns time period simulated. The dynamics of the rotor is characterized by a librational motion in the potential well. The frequency of the librational mode obtained from Fourier analysis of the computed motions is 500 ± 100 GHz, in good agreement with a frequency of 475 GHz obtained by a harmonic fit to the potential curve at the minimum angle. The rate of jumps over the barrier increases with the temperature. None were observed within 0.5 ns at 10 K, and 14 were observed at 300 K. At 400 K and above, kT exceeds V_b and we found irregularly alternating periods of bidirectional rotation and libration in the potential well.

Rotating Electric Field Applied. (i) Torsional Barriers Suppressed. This artificial case is particularly simple. We examined it by turning off all nonbonding interactions (van der Waals and electrostatic) between atoms separated by more than three bonds. The resulting torsional potential has barriers lower than 0.1 kcal/mol. The dominant feature in the Fourier transforms (Figure 9) of the sine of the time dependent rotor angle occurs at the applied frequency ω of the electric field as long as the field E is strong enough for the rotor to follow. At sufficiently strong field, a second signal in the Fourier transform occurs at a frequency ν' proportional to $E^{1/2}$, $\nu' = (2.53 \pm 0.32)$ GHz $\times$ $(E/\mathrm{MVcm^{-1}})^{1/2}$. A higher harmonic appears very weakly at $2\nu'$.

(ii) Torsional Barriers Present. The torsional potential for the rotor of Figure 3 is shown in Figure 4. If E is not excessive, the Fourier transforms of nearly all simulations show two common features: a strong signal between 0 and 500 GHz, and a second, weaker one between 1000 and 2500 GHz. Figure 10 shows the Fourier transforms obtained from simulations A−G. At low electric fields (runs B−F), they resemble the Fourier transform from the simulation without applied electric field (run A). The electric field strength in run G is much higher than the

Table 2. Rotor Characteristics from Representative Simulations[a]

	T_{sys} (K)	E (MV/cm)	ν (GHz)	T_{eq} (K)	T_{fluc} (K)	T_{tot} (K)	T_{rot} (K)	a
A	500			521	517	477	385	
B	500	5	500	643	589	468	394	0.85
C	100	10	1250	652	496	154	136	0.85
D	500	25	500	2323	807	539	455	0.06
E	10	20	650	960	667	48	42	0.77
F	10	20	750	430	415	45	39	0.98
G	10	1	500	14	14	10	8	1.00
H	20	10	10	51	50	19	15	0.01

[a] T_{sys} is the system temperature, T_{eq} is the temperature equivalent of the rotational energy of the rotor, T_{fluc} is the temperature of fluctuations of the rotational energy of the rotor, T_{rot} is the rotational temperature, and T_{tot} is the rotor's total temperature in the rotating frame. E and ν are field strength and frequency of the applied electric field, and a is the average lag per turn. For mathematical definitions, see the section Computational Procedures.

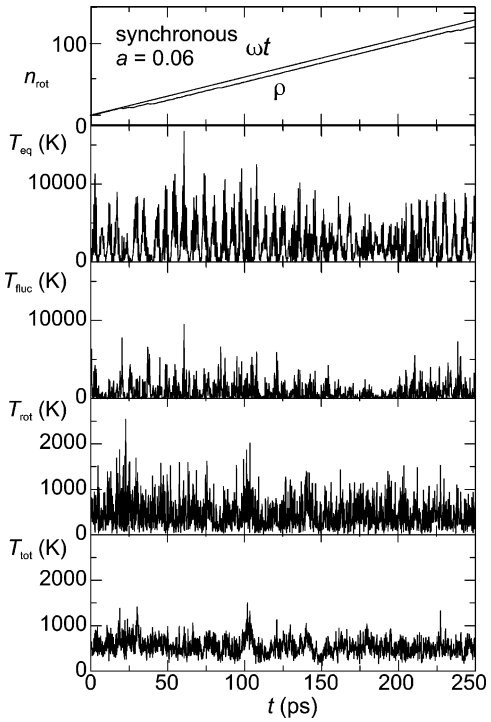

Figure 5. Example of synchronous rotor behavior (run D in Table 2); n is the number of turns.

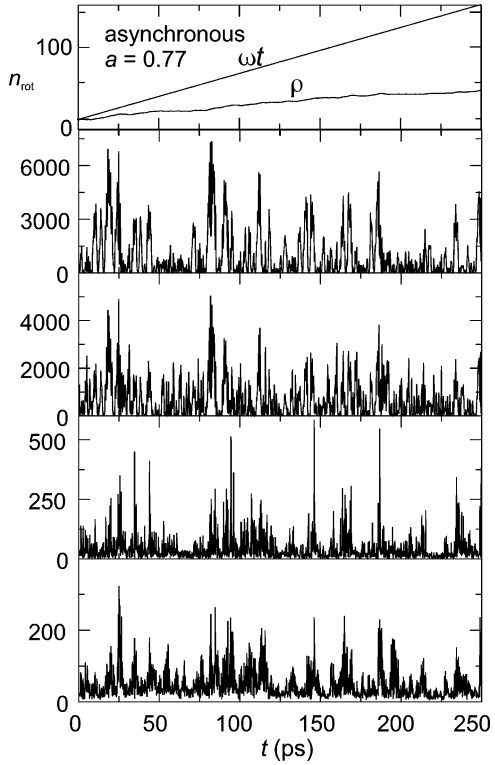

Figure 6. Example of asynchronous rotor behavior (run E in Table 2); *n* is the number of turns.

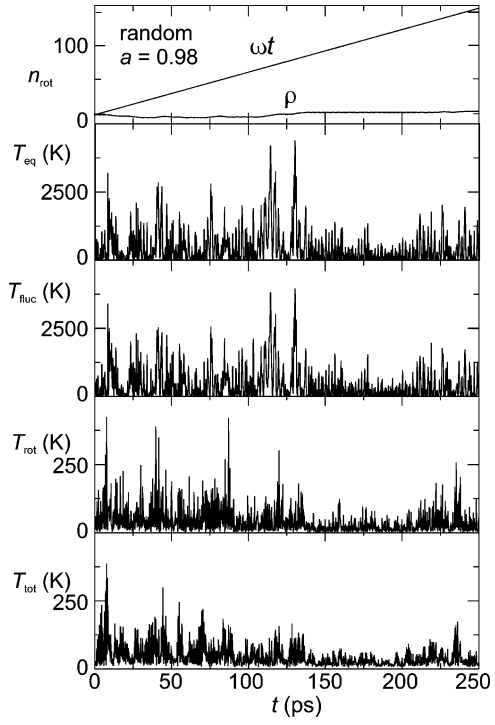

Figure 7. Example of random rotor behavior (run F in Table 2); *n* is the number of turns.

torsional barrier and the Fourier transform has the same characteristics as those obtained when torsional barriers were suppressed.

We frequency analyzed the rotor motion by first Fourier transforming the rotor coordinates, selecting a frequency range, and back transforming only the coefficients within this range. Rotational motion was found to occur in a broad frequency

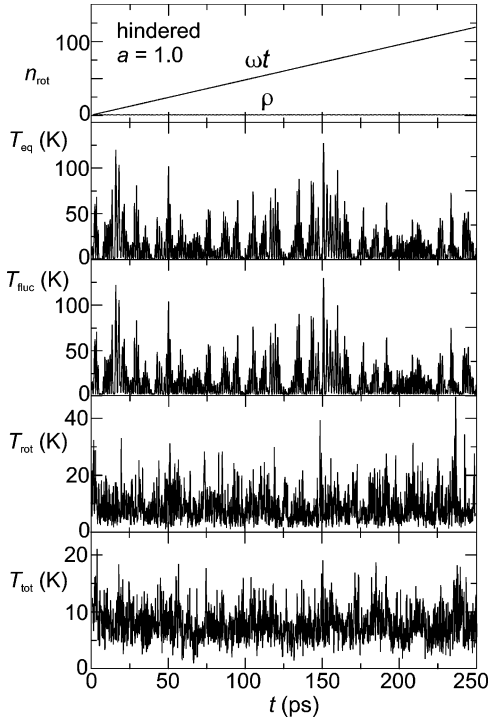

Figure 8. Example of hindered rotor behavior (run G in Table 2); *n* is the number of turns.

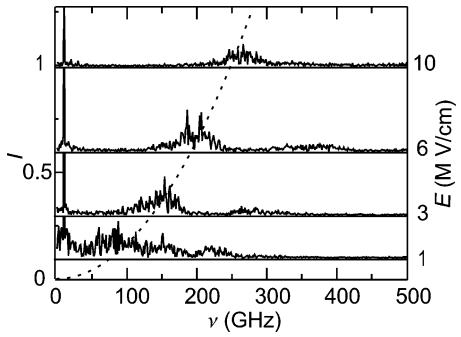

Figure 9. Fourier transforms of the sine of the rotor angle, sin $\rho(t)$, for simulations without rotor-surface interaction at $\nu = 10$ GHz.

range, 500 ± 100 GHz. Librational motion occurs over an even broader frequency range, centered at similar frequencies as the rotation.

Phase Diagrams of Rotor Motion. We used a previously proposed[10] classification scheme (Figures 4−7) to describe the response of the molecular rotor to the driving electric field based on the average lag per turn, *a*. When *a* is equal to zero, the rotor motion is in phase with the electric field, and no turns are skipped. With increasing *a* the rotor skips an increasing fraction of the turns of the field. For $a < 1/e$, the rotor motion is said to be synchronous, for $a > 1/e$, asynchronous. Beside these two regimes, where the induction of directional rotational motion is successful ($a < 1$), three more were proposed when $a \approx 1$. If the rotor is trapped in a potential minimum and executes only a librational angular motion, it is said to be in the hindered regime. If transitions over the torsional barrier occur and the rotor performs a random motion without significant directional preference, the regime is called random thermal if $E < kT/\mu$, and random driven otherwise. The minimum field strength required to obtain synchronous rotation is defined as the critical field, E_c, and the weaker one required to secure asynchronous

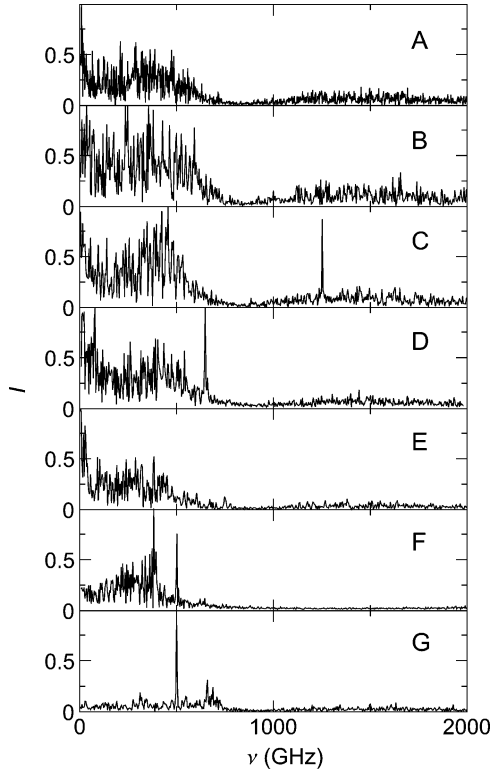

Figure 10. Fourier transforms of the sine of the rotor angle, sin $\rho(t)$, for simulations A−G in Table 2.

rotation as the breakoff field, E_{bo}. The regime of motion of a rotor depends on three variable parameters: the temperature T, and the frequency ν and amplitude E of the rotating electric field.

The regimes of rotor motion can be displayed in a phase diagram. For a given rotor, and thus a fixed rotational barrier and moment of inertia, and for a given temperature, the critical and the breakoff field strengths are plotted against the frequency of the electric field on a log−log scale. Figure 11 shows three phase diagrams. One was obtained at 10 K, where $kT = 0.02$ kcal/mol is much lower than the torsional barrier $V_b = 0.75$ kcal/mol, one at 300 K, where $kT = 0.59$ kcal/mol is just below V_b, and one at 500 K, where $kT = 0.99$ kcal/mol exceeds V_b. At 10 and 300 K, E_{bo} and E_c do not depend detectably on frequency below 500 GHz, and we found the approximately constant values $E_{bo} \approx 5$ MV/cm and $E_c \approx 10$ MV/cm for $\nu <$ 500 GHz. Above 500 GHz, E_c and E_{bo} are approximately quadratic functions of ν (a slope of two in the log−log plot of Figure 11). All this is similar to what was computed for another rotor before.[10] In the 500 K phase diagram, $E_{bo} \approx 6.5$ MV/cm and $E_c \approx 14$ MV/cm up to ∼550 GHz. Above this value both again increase quadratically. However, at all three temperatures, starting at 1000 GHz E_{bo} gradually decreases to the value that it has below 500 GHz, whereas E_c continues to increase regularly. In that case, the rotor motion is characterized by periods of directional rotation at a frequency of 500 GHz regardless of the electric field frequency, interrupted by periods of random motion.

A Simple Steady-State Model for Rotor Motion. To analyze the phase diagrams that resulted from molecular dynamics simulations, we elaborate the simple model for the response of a molecular rotor to rotating electric field that was developed previously.[10] We do so by adding an explicit

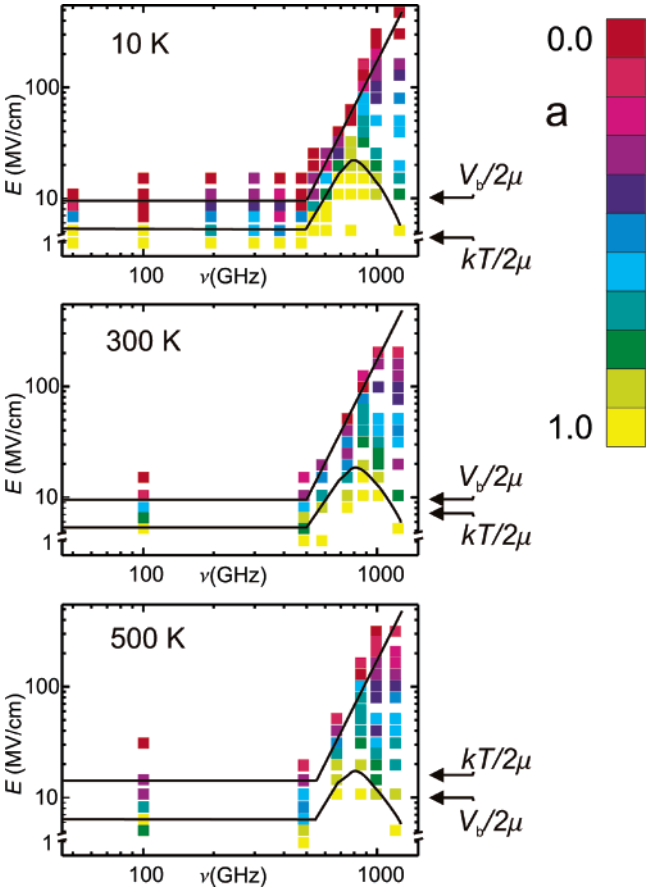

Figure 11. Phase diagrams of rotor motion at 10, 300, and 500 K, displaying the values of $a(E,\nu)$ at the points which correspond to the simulation conditions. The estimated lines of E_c and E_{bo} are shown in black.

consideration of the torsional barrier, which was negligible for the situation analyzed earlier. In a steady state, the rotor can be described[16] by the Langevin equation

$$I\partial^2\rho(t)/\partial t^2 = -\mathrm{d}V_{\mathrm{eff}}(\rho)/\mathrm{d}\rho - \eta\partial\rho(t)/\partial t + \zeta(T,t) \qquad (1)$$

where $\zeta(T,t)$ is a stochastic force representing thermal fluctuations in the system.

Zero Temperature. At first, we assume $T = 0$ and, thus, no stochastic force. Previously,[10] in the case of constant torsional potential, by identification of V_{eff} with $-E\mu$, a condition for sin α was derived using the steady-state approximation. In steady state the total torque on the rotor vanishes. The friction torque is equal and opposite to the electric field torque, and the lag angle α is constant. Without torsional barriers α is thus given by[10]

$$\sin\alpha = 2\pi\eta\nu/\mu E \qquad (2)$$

With increasing lag angle α the torque produced by the electric field increases until it reaches a maximum at $\alpha = \pi/2$. The requirement for faithful rotor following, $\alpha < \pi/2$, produces a value for the strength of the break-off field, E_{bo}

$$E_{bo} = 2\pi\eta\nu/\mu \qquad (3)$$

Presently, we need to include the torque $-\partial V(\rho)/\partial\rho$ caused by the intrinsic torsional potential into the steady-state assumption. The lag angle is then

$$\sin \alpha = (2\pi\eta\nu + \partial V/\partial\rho)/\mu E \quad (4)$$

During each turn, the crucial point for potentially skipping a turn occurs when the torsional potential increases most steeply, and the requirement for faithful rotor following is

$$E_{bo} = [2\pi\eta\nu + (\partial V/\partial\rho)_{max}]/\mu \quad (5)$$

We approximate the 1-fold torsional potential of the rotor studied (Figure 4) by a cosine function

$$V(\rho) = (V_b/2)\cos\rho \quad (6)$$

This is a crude assumption, but reproduces the important features of the potential reasonably well. For this potential, $[\partial V(\rho)/\partial\rho]_{max}$ equals $V_b/2$, and the breakoff field is

$$E_{bo} = 2\pi\eta\nu/\mu + V_b/2\mu \quad (7)$$

In the limiting case of no intrinsic barrier, $V_b = 0$, we recover the previously[10] described equation for E_{bo}. Then, the potential governing the rotor motion in the frame rotating at frequency ω is time independent and has the appearance of a tilted washboard.

Temperature Effects. At 0 K, the rotor either follows synchronously or not at all ($E_c = E_{bo}$). For $T > 0$ the stochastic force term $\zeta(T)$ in eq 1 does not vanish. Solving the Langevin equation will produce the correct dynamics within the model, thus yielding values for a at given T, E, and ν. Instead, in our search for qualitative insight, we extend the simple model. The dynamic effects caused by the inertia of the rotor angular motion are likely to be relatively small, since its moment of inertia is small, and shall be ignored in the present steady-state model. This approximation might be poorer for larger rotors, such as some of those examined in the past,[9,10] and we intend to revisit this issue in the future.

As before,[10] we attribute asynchronous rotation to thermally activated jumps over the torsional barrier. A schematic plot of the rotational potential V in the rotating frame at two instants in time is shown in Figure 12. It contains the dipole energy in the electric field, friction, and the intrinsic torsional potential

$$V(\alpha,\rho) = \mu E\cos\alpha - \eta\omega\alpha + (V_b/2)\cos\rho \quad (8)$$

The potential is not 2π-periodic, since the friction term does not represent a conservative force. The barrier on the left represents forward jumps, when the rotor turns faster than the electric field frequency. Jumps over the barrier on the right mean that the rotor skips turns. Because of friction, the right barrier is lower than the left one, and the probability of jumps to the right exceeds the probability of those to the left. Using the Arrhenius equation, a simple expression for the average lag angle a as a function of the friction constant $\eta(\nu)$ was obtained previously[10] in the absence of an intrinsic barrier.

This expression for a has to be modified when an intrinsic torsional potential is present, since it causes the rotational potential in the rotating frame to be modulated in time. Because this modulation frequency ω is assumed to be much slower than the attempt frequency ($\sim 10^{13}$ s^{-1}), we average the instantaneous rates p_r and p_l over the length of a period. We have not found an analytical form for averaged rates P_r and P_l, and have developed an approximate procedure instead (Appendix). Explicit albeit approximate expressions for P_r and P_l are thus available.

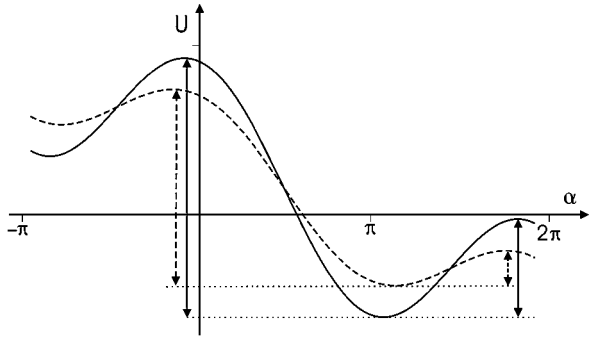

Figure 12. Rotational potential U in rotating frame for modulation angle $\varphi = \omega t$ equal to 0 (full line) and π (dashed line). The arrows show the left and right torsional barriers ΔU in each case.

As before,[10] the average lag a is equal to

$$a = (P_l - P_r)/(\nu + P_l - P_r) \quad (9)$$

Discussion

Quartz Glass Surface Model. We find a slightly excessive density, 2.5 g/cm^3, compared to the experimental value found for bulk quartz glass, which is 2.2 g/cm^3.[37] Peaks in the radial distribution functions are at distances ~10% shorter than literature values[38] obtained with the BKS potential developed for the study of silica systems.[39] In our calculation of the angle distribution functions we did not distinguish between the surface and the interior of the glass. The maximum for the O−Si−O angle is in good agreement with literature results,[38] the maximum for Si−O−Si is between the maxima found for the surface (130°) and for the interior (150°).[38] Clearly, our quartz glass model is rather crude. However, in our study we are interested in the properties of the attached molecular rotor, and the quartz glass serves only as a carrier to which the rotors are mounted. Although a study of intrinsic glass properties would require additional refinement, we believe that the structure is good enough for our purposes.

Surface-Mounted Rotor. The variation in the torsional potentials from one rotor position to another that we observed in our simulations is an effect of surface inhomogeneities. The torsional barriers of rotors on surface II are higher than those of rotors on surface I. This is most likely due to nonbonding interaction of the rotors with the methyl groups on the surface.

We analyzed van der Waals (vdW) and electrostatic contributions to the torsional potentials separately. The electrostatic energy is approximately sine shaped, thus indicating that a dipole-electric field approximation of the electrostatic rotor-surface interaction is a valid choice. The vdW energy has two or three minima for some rotors, where the lowest minimum occurs at the same angle as the electrostatic minimum. We attribute the existence of potentials with one, two, or three minima to a variation in the polar angle ξ of the rotor (defined in Figure 3). For an ideally mounted rotor ($\xi = 90°$) the torsional barrier would most likely be very small. Due to the amorphous

(37) *Handbook of Chemistry and Physics*, 67th ed.; Weast, R. C., Ed.; CRC Press: Boca Raton, 1986.
(38) Roder, A.; Kob, W.; Binder, K. *J. Chem. Phys.* **2001**, *114*, 7602.
(39) van Beest, B. W. H.; Kramer, G. J.; van Santen, R. A. *Phys. Rev. Lett.* **1990**, *64*, 1995.

nature of the surface, real rotors are inclined ($\xi < 90°$). If ξ does not deviate much from 90°, a torsional barrier arises from the electrostatic interaction and the van der Waals attraction of the chlorine atom to the surface. The vdW attraction of chlorine is stronger than that of the hydrogen atoms, and governs the vdW potential shape when ξ is close to 90°. Then, only the chlorine atom gets close enough to the surface to be attracted to it significantly, and the potential is "1-fold", with a single minimum. If the rotor is tilted strongly ($\xi \ll 90°$), the interactions become more complicated. At certain rotor orientations, the hydrogen atoms can now also interact with the surface, and the vdW potential has two or three minima.

In a previous study,[11] we compared the torsional barriers of the shorter chloromethyl rotors, $(-O)_3SiCH_2Cl$, obtained by the same molecular modeling procedure, with measured barrier heights. We found that the calculated barrier height distribution was shifted to higher values than the observed one. We took this as an indication that in the experimental sample the rotors in the grown silica layer were closer to perpendicular to the surface ($\xi \approx 90°$) than our modeling suggested, and we can expect a similar situation here. The lower values of the previously observed barriers might also result from more substantial differences between the real nature of the rotor-coated surface and the structures assumed. For instance, in the experiments unknown amounts of adsorbed impurities such as water may have been present. Our present goal is to unravel the fundamentals of the dynamical behavior of the rotor with a particular potential barrier as a function of temperature and field strength and frequency, and we expect these to be largely independent of the detailed surface structure. A realistic modeling of any particular experimental surface will require additional work.

Rotational Behavior. Application of a rotating electric field adds a $\mu E \cos \omega t$ term to the torsional potential. If the energy of interaction with the electric field is much larger than the torsional barrier, the effective torsional potential can be approximated by a time independent cosine potential in a coordinate system rotating at the same frequency as the electric field.[10] We expect two contributions to the angular motion. Beside the dominant synchronous following at the frequency $\nu = \omega/2\pi$, there is thermal librational motion within the potential produced by the applied field at the frequency ν'. The curvature of the potential is μE, and the librational frequency ν' in this potential is expected to be $(\mu E/I)^{1/2}/2\pi$. This is in excellent agreement with the simulation data in the absence of torsional barriers (Figure 9). For example, at 10 MV/cm the theoretical value of ν' is 270 GHz, and the simulation yields 260 ± 20 GHz.

The presence of significant torsional barriers complicates the situation. Now the effective torsional potential in the rotating frame is the potential due to the electric field modulated by the time-dependent intrinsic potential (Figure 12). With the modulation, the shape and the curvature of the potential minimum change, consequently time independent eigenfrequencies do not exist. Instead, the librational motion occurs in a broad frequency range (Figure 10). With increasing field strength the time-dependent potential modulation in the rotating frame becomes less pronounced, and the character of the rotor motion gradually shifts toward the case of no significant torsional barrier (entry G in Figure 10).

Rotor Temperatures. If no electric field is applied, the rotor is in thermal equilibrium with its environment. The temperatures $\langle T_{eq} \rangle$ and $\langle T_{fluc} \rangle$, which are equivalent because the rotor executes no net directional motion, are roughly equal to T_{sys}. The temperatures $\langle T_{tot} \rangle$ and $\langle T_{rot} \rangle$ are lower than T_{sys}, because their definition includes only a part of the motion related to each degree of freedom. If an electric field is applied, energy is delivered to the rotational mode of the rotor, and the ratio of $\langle T_{eq} \rangle$, $\langle T_{fluc} \rangle$, $\langle T_{tot} \rangle$, and $\langle T_{rot} \rangle$ to T_{sys} increases. If directional motion is induced, $\langle T_{eq} \rangle$ represents the energy of a driven motion in addition to thermal contributions, it exceeds $\langle T_{fluc} \rangle$, and both exceed $\langle T_{sys} \rangle$ and $\langle T_{rot} \rangle$.

The claim that in a rotating electric field the dipolar rotor acts as energy absorbing antenna is supported by the results of two simulations performed at 10 K, 500 GHz, and 15 MV/cm, in one of which the chloropropynyl rotor was replaced by a methyl group. No thermostat was applied. The system containing the polar rotor group showed a heating rate of 5 K/ns, 10 times higher than the rate of 0.5 K/ns observed for the system without the polar rotor. The small six atom rotor absorbs 10 times more energy than the other ~3500 atoms of the system. Clearly, the excitation preferentially pumps the rotational motion as intended and this produces the high values of T_{eq} in Table 2.

When the rotor follows the field synchronously, T_{eq} shows a distinct modulation, which appears to be related to the oscillations in the potential provided by the rotating field observed in the absence of the torsional barrier, at a frequency of $(\mu E/I)^{1/2}/2\pi$, as discussed above. The exact nature of this modulation is still unclear, and we hope to elucidate it in the future.

Phase Diagram. The simple model accounts well for the general features of the phase diagram (Figure 11). Below 500 GHz, the simulation data show very little frequency dependence, because at these frequencies, friction is not the limiting factor resisting directional rotation. Instead, at low temperatures the driving force fights the torsional barrier and at higher temperatures it fights Brownian motion. Only at frequencies higher than about 500 GHz the driving force fights friction, and the simulation runs obtained at these frequencies can be used to deduce the friction constant by determining the friction energy term $-\eta\omega\alpha$ in eq 8.

Most of the lines separating regimes of behavior in the phase diagram (Figure 11) have simply understandable origin.

(i) When $kT < V_b$, E_{bo} is given by eq 7. Below 500 GHz the friction term is small compared to V_b and $E_{bo} \approx V_b/2\mu$, and it is the cogging effect of the intrinsic barrier that has to be overcome by the electric field. In the phase diagrams at 10 and 300 K obtained from the numerical simulations, $E_{bo} \approx 5$ MV/cm. Identifying μ with the dipole moment component perpendicular to the Si−C bond, the expected value for E_{bo} is 4.6 MV/cm, slightly lower than the observed value. A higher observed value for E_{bo} is consistent with a lower value for μ_{xy}, expected if the rotor is tilted ($\xi < 90°$). The component of the dipole moment perpendicular to the z-axis is given by $\mu \sin \xi$, and from the observed E_{bo} value we obtain $\xi = 67°$. We monitored ξ during one arbitrarily chosen simulation and found an average value of $\langle \xi \rangle = 70°$, in good agreement.

(ii) When $kT > V_b$, the simulations yielded $E_{bo} \approx 6.2$ MV/cm, a value roughly equal to the expected value of $kT/2\mu$,

Table 3. Values for the Friction Constant η Obtained by a Fit of eq 9 to the Simulation Results at Different Temperatures and Frequencies

	10 K	100 K	200 K	300 K	400 K	500 K
500 GHz	0.02	0.04	0.04	0.05	0.04	0.05
650 GHz	0.91	0.21	0.26	0.22	0.27	0.28
750 GHz	1.59					
875 GHz	2.66	2.68		2.52		2.04

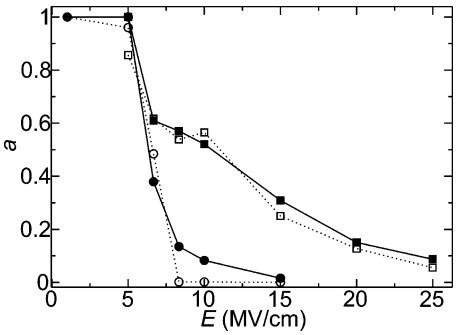

Figure 13. Average lag $a(E)$ from simulations and from a fit to eq 9. ○: 500 GHz, 10 K, simulation data; ●: 500 GHz, 10 K, fitted; □: 500 GHz, 500 K, simulation data; ■: 500 GHz, 500 K, fitted.

6.7 MV/cm. In this case, it is the thermal motion that has to be overcome by the electric field.

(iii) As frequency increases, the friction term in eq 7 is expected to take over, and indeed, this is the behavior observed in the phase diagram. From the intercept and slope of the observed phase boundary, we can deduce the value of $\eta(\nu)$.

Fitting of the Friction Constant η. Examination of the results for P_r and P_l derived in the Appendix shows that the only undetermined parameter in eq 9 for a is the friction constant η, which enters through the terms $B_{l,r}$ and C in eq 20. These contain c_f, which is proportional to η, cf. eq 11. Values for η can be obtained by fitting a to the values obtained from the simulations. For every frequency at 500 GHz and above and for each temperature we obtained a value for η by fitting $a(E)$ to the simulation data. The fits are very satisfactory and Table 3 shows a compilation of the resulting values of $\eta(T,\nu)$. In contrast to an ideal macroscopic rotor, for which the friction constant η is frequency independent, the friction constant of the molecular rotor varies with frequency. Examples of fits are given in Figure 13, which shows $a(E)$ obtained from the simulation data and from the fitting at 500 GHz for 10 and 500 K. Within the margins of error, η is temperature independent (Figure 14A). The slightly different values for different temperatures were therefore averaged to obtain a temperature independent friction constant η as a function of frequency (Figure 14B). Between 500 and 1000 GHz η is an approximately linear function of ν, and linear regression gives $\eta = 0.26$ ps eV $\times$ $(\nu - 0.5)$/THz.

However, at 1000 GHz, the friction constant as defined through eq 9 decreases again, due to the decrease of E_{bo} in the phase diagrams (Figure 11). This occurs in the frequency range where we find a second weak signal in the Fourier transforms of the rotor angle (cf. Figure 10). The relation of the frequency dependence of the friction constant to rotor structure promises to be interesting to examine after data for a few additional molecular rotors are acquired.

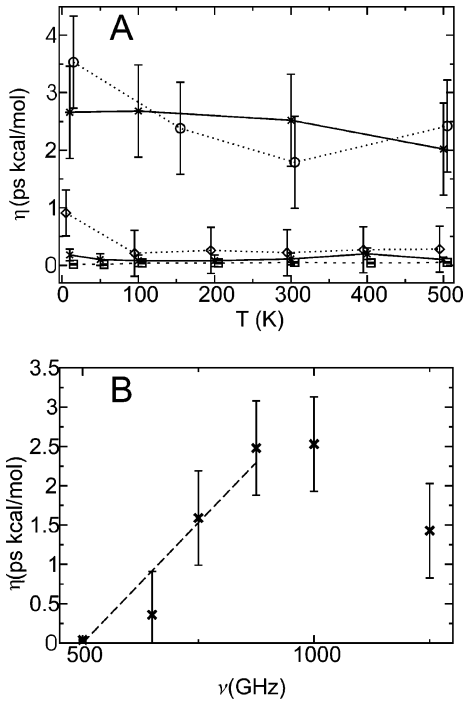

Figure 14. A: Plots of friction constant η versus temperature for different electric field frequencies ν. ×: 100 GHz; □: 500 GHz; ◇: 650 GHz; ∗: 875 GHz; ○: 1000 GHz. B: Plot of friction constant η versus electric field frequency ν.

Nature of Friction. We propose that the physical origin of the friction described by the friction constant η is the loss of energy from the rotational mode to all other modes of nuclear motion in the system by intramolecular vibrational relaxation. We have already pointed out above that almost all the energy absorbed from the electric field is used to pump the rotational motion. In the steady state attained, the rate of pumping must equal the rate of energy loss to the rest of the system, and it is only logical to identify the rate of the energy loss with the friction experienced by the driving force.

To demonstrate the existence of this energy loss, we have examined the decay of rotational excitation in simulations in which the rotating electric field was turned off suddenly while the rotor motion was in the synchronous regime. This was done at several frequencies at 10 K. The strength of the electric field used exceeded E_c. After the field was turned off, the rotor motion rapidly became random. Relaxation times were obtained for T_{eq}, T_{rot}, and T_{tot} through fits assuming exponential decay, and they were all in the range of a few ps. This fast relaxation shows that the rotational energy of the driven rotor in excess of kT is distributed rapidly among the vibrational states of the whole system, by coupling through the electric field and/or kinematic interactions. There is no reason to assume that a similar mechanism for energy dissipation fails to operate while the electric field is on and the rotational excitation of the rotor remains roughly steady.

In principle, the values for the friction constant η can be derived from the observed relaxation times. However, these relaxation times appear to be widely distributed, and much averaging would be necessary, requiring many individual simulations. We prefer to derive the values of η from steady-state simulations, where averaging over the time of the simulation is automatic.

Summary

We studied the effect of rotating electric fields on the 3-chloroprop-1-ynyl rotor, $(-O)_3SiC{\equiv}CCH_2Cl$, mounted on an amorphous quartz glass surface. A rotor mounted at five different sites on one model surface experiences torsional barriers between 0.65 and 2.5 kcal/mol, and on another model surface, torsional barriers between 0.8 and 3.0 kcal/mol. One rotor position was studied in detail by classical molecular dynamics and the rotor's ability to follow the electric field was evaluated. The numerical results were analyzed using a simple steady-state model that includes the electric field (the driving force), thermal motion, the rotor's torsional potential (cogging), and friction. Different regimes of rotational motion were characterized by phase diagrams at three different temperatures. For synchronous following the electric field has to be higher than the critical field strength E_c and for asynchronous following it has to be larger than the somewhat lower breakoff field E_{bo}. At frequencies at which the dipole-field interaction energy at the breakoff field, $2\mu E_{bo}$, is smaller than either kT or V_b, E_{bo} and E_c are nearly frequency independent, and the driving force fights either the intrinsic barrier, i.e., cogging at low temperatures ($kT < V_b$), or random thermal motion at high temperatures ($kT > V_b$). Under these condition, the friction constant η is irrelevant. When $2\mu E_{bo}$ exceeds both kT and V_b, the driving force fights friction, characterized by the frequency-dependent friction constant η, and both E_{bo} and E_c increase approximately quadratically with frequency. For E_{bo}, this increase is interrupted at very high frequencies above 1000 GHz by a broad resonance of the electric field and internal rotor motions where friction is smaller again and E_{bo} decreases to the value found below 500 GHz. In the region between 500 and 1000 GHz, η is given by 0.26 ps eV $\times$ ($\nu - 0.5$)/THz. The friction constant η is most simply interpreted as describing the rate at which energy escapes from the mode of motion driven by the external field (rotation) into other degrees of freedom and is thus closely related to IVR (intramolecular vibrational redistribution).

Although the concepts derived above were deduced for a particular case of a very simple dipolar rotor, we expect that they will be applicable generally. In particular the notion that the driving force needs to contend with friction, random thermal motion, and cogging (intrinsic barriers), depending on the frequency of operation and on temperature, is likely to apply generally.

Acknowledgment. We thank Dr. Laura I. Clarke, Prof. John C. Price, and Prof. Charles T. Rogers for helpful discussions. This work was supported by the U.S. Army Research Office (DAAD19-01-1-0521). D. H. thanks the Alexander von Humboldt Foundation for a Feodor Lynen fellowship.

Appendix:

Derivation of Time-Averaged Thermal Jump Rates. The general expression for the potential energy V of the rotor is a sum of the electric field contribution, the friction term, and the intrinsic barrier, eq 8, where ρ is the rotor's orientation angle and α its lag behind the electric field. The expression for the friction term is in analogy to the steady-state model at 0 K, where increasing friction causes increasing values of α. The angles α and ρ are related by $\alpha = \rho - \omega t$. While α is constant if the rotor motion is perfectly synchronous with the electric field, ρ is constant if the rotor does not rotate ($\rho = \rho_0$). Our model for asynchronous rotation starts with synchronous rotation ($\rho = \rho_0 + \omega t$), and the mathematical treatment of eq 8 is simplified in a coordinate system rotating at the frequency of the electric field, where α is the natural coordinate. Defining $\varphi = \omega t$ as the source of time dependent modulation, we express V as a function of α and φ

$$V(\alpha,\varphi) = \mu E \cos\alpha - \eta\omega\alpha + (V_b/2)\cos(\alpha + \varphi) \quad (10)$$

We define reduced parameters c_f and c_i and a reduced potential U

$$c_f = \eta\omega/\mu E \quad (11)$$

$$c_i = V_b/2\mu E \quad (12)$$

$$U(\alpha,\varphi) = V(\alpha,\varphi)/\mu E = \cos\alpha - c_f\alpha + c_i\cos(\alpha + \varphi) \quad (13)$$

The parameters c_f and c_i are positive by definition, and determine the shape of $U(\alpha,\varphi)$. We distinguish three cases

(i) Friction Dominated, $c_f > |c_i - 1|$. For some values of φ, $U(\alpha)$ has no minimum. The angle α increases with the simulation time, as the rotor aims toward lower values of U without limit. The rotor will not follow the electric field, and $a \approx 1$.

(ii) Intrinsic Barrier Dominated, $c_i > 1 + c_f$. $U(\alpha)$ has a minimum for all φ. The minimum follows the intrinsic potential, which is constant in the space fixed coordinate system. In the rotating frame, the minimum moves toward higher values of α without limit as the simulation time increases. The applied electric field does not induce directional rotational motion, and $a \approx 1$.

(iii) Electric Field Dominated, $c_f + c_i < 1$. Again, $U(\alpha)$ has a minimum for all φ. Now the minimum follows the electric field, and its position is nearly constant in the rotating frame. The rotor stays in the minimum, except possibly for occasional thermally activated jumps, and $a < 1$.

Figure 12 shows $U(\alpha)$ for $\varphi = 0$ and $\varphi = \pi$ in the electric field dominated case. The spontaneous transition rates are $p = A\ e^{-\Delta V/kT}$, where ΔV is the barrier height of $V(\alpha)$, assuming that the field frequency ν is much lower than the frequency factor A, which is taken equal to $10^{13}\ s^{-1}$. To account for the modulation of ΔV in time, averaged transition rates are calculated. They are defined as

$$P = \int_0^{2\pi} p(\varphi)\mathrm{d}\varphi / \int_0^{2\pi} \mathrm{d}\varphi \quad (14)$$

where the integral is over one turn of the electric field. A straightforward evaluation of $\Delta U(\varphi)$, the barrier height of the reduced potential, yields complicated expressions, and the integration of p has to be performed numerically. To simplify the calculation of P, we present an approximate treatment. Figure 15A shows a contour plot of $U(\alpha,\varphi)$ and a plot of $\Delta U(\varphi)$ for representative values of c_f and c_i. Even though $U(\alpha,\varphi)$ is not symmetric with respect to the symmetry operation $\varphi \rightarrow \pi - \varphi$, the relation $\Delta U(\varphi) = \Delta U(2\pi - \varphi)$ is valid. The integration to obtain P can therefore be done over $\varphi \in [0,\pi]$.

To find a simple expression for the time dependent barrier, two limiting cases are considered:

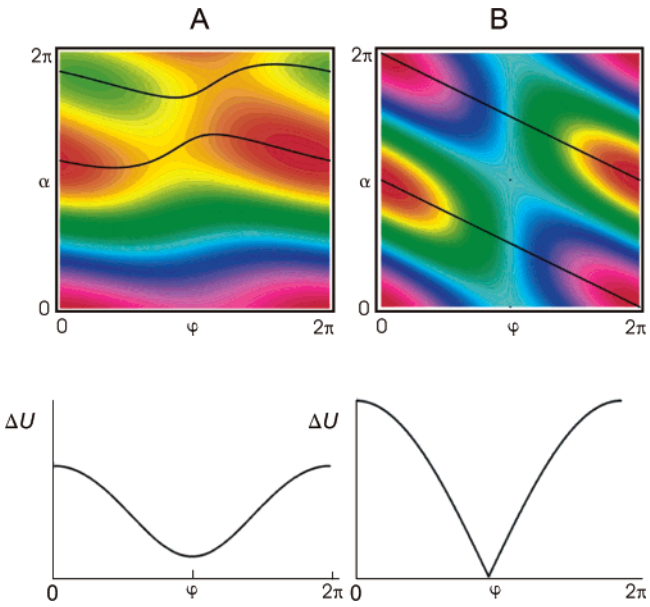

Figure 15. Contour plots of the reduced potential U (eq 13) and plots of the reduced barrier height ΔU; α is the lag angle and $\varphi = \omega t$ is the modulation angle. A: $c_f = 0.25$, $c_i = 0.5$. B: $c_f = 0$, $c_i = 1$.

(i) $c_f = 0$, $c_i = 1$. In this case the potential has the form $U(\alpha,\varphi) = \cos\alpha + \cos(\alpha + \varphi)$. A contour plot of U and a plot of ΔU are shown in Figure 15B. The expressions for the minimum and maximum are $\alpha_{min} = \pi - \varphi/2$ and $\alpha_{max} = 2\pi - \varphi/2$. The barrier height is then

$$\Delta U(\varphi) = U(\alpha_{max},\varphi) - U(\alpha_{min},\varphi) = 2\cos\varphi/2 \quad (15)$$

In this case, the integration in eq 14 to obtain P can be done analytically. If we write $\Delta U(\varphi) = B + C\cos\varphi/2$, we obtain for arbitrary B and C

$$P = A\,e^{-B}\,[I_0(C) - L_0(C)] \quad (16)$$

where I_0 is the modified Bessel function of first kind of order zero and L_0 is the modified Struve function of order zero.[40] At the moment, $B = 0$ and $C = 2$. When we solve the general case, the factors B and C will acquire other values.

(ii) $c_f > 0$, $c_i \to 0$. If $c_i = 0$, then the potential is not modulated in time, the averaging becomes unnecessary, and we revert to the case published previously.[10] For small values of c_i, the barriers are still modulated, but we can assume that the positions of α_{min} and α_{max} are independent of φ and are related by $\alpha_{max} = \pi - \alpha_{min}$. The potential is given by eq 10 and the potential barrier becomes

$$\Delta U(\varphi) = c_f(2\alpha_{min} - \pi) - 2\cos\alpha_{min} - 2c_i\cos\alpha_{min}\cos\varphi \quad (17)$$

This can be written as $\Delta U(\varphi) = D + F\cos\varphi$, where $D = c_f(2\alpha_{min} - \pi) - 2\cos\alpha_{min}$ and $F = -2c_i\cos\alpha_{min}$. Again, the general case will require other values for D and F. Analytical integration of eq 14 now yields

$$P = A\,e^{-D}\,I_0(F) \quad (18)$$

In the two limiting cases discussed so far, (i) and (ii), the expression for $\Delta U(\varphi)$ contains in one case $2\cos\varphi/2$ and, in the other case, a constant plus a multiple of $\cos\varphi$. In the general case where $c_f + c_i < 1$, the shape of $\Delta U(\varphi)$ is intermediate between the two limiting cases, and it is reasonable to assume that the averaged transition rate is described by the linear combination

$$P = A\{q\,e^{-B}\,[I_0(C) - L_0(C)] + (1 - q)\,e^{-D}\,I_0(F)\} \quad (19)$$

where B, C, D, and F are defined by the values of $\Delta U(\varphi = 0)$ and $\Delta U(\varphi = \pi)$:

$$B_{l,r} = \left[2\sqrt{(1 - c_i)^2 - c_f^2} \pm c_f\pi + 2c_f \arcsin\frac{c_f}{1 - c_i}\right]/c_T$$

where $+$ applies for B_l and $-$ applies for B_r

$$C = \left[2\sqrt{(1 + c_i)^2 - c_f^2} - \sqrt{(1 - c_i)^2 - c_f^2} + 2c_f\left(\arcsin\frac{c_f}{1 + c_i} - \arcsin\frac{c_f}{1 - c_i}\right)\right]/c_T \quad (20)$$

$$D_{l,r} = B_{l,r} + C/2$$

$$F = C/2$$

where we have introduced c_T in analogy to c_f and c_i: $c_T = kT/\mu E$. The subscript l or r on B and D specifies whether the expression refers to the left or right potential barrier; B_l (D_l) and B_r (D_r) differ by $2c_f\pi$. C and F are identical for the two barriers, because $\Delta U(2\pi + \varphi) = \Delta U(\varphi) - 2c_f\pi$ for all φ. The parameter q is the only undetermined quantity required to evaluate P and it is a measure of the $\cos\varphi/2$ character of $\Delta U(\varphi)$. We have not found an analytical expression for it. We calculated the real values of P by numerical integration for a set of c_i, c_f, and c_T values. Using eq 19 we obtained a value for q at each point and found that the simple expression $q = c_i$ fits the data quite well, whereas the dependence of q on c_f and c_T is negligible.

JA0348851

(40) Gradshteyn, I. S.; Ryzhik, I. M. *Tables of Integrals, Series, and Products*; Academic Press Inc.: Orlando, 1980.